CEAS Aeronaut J (2017) 8:441–460
DOI 10.1007/s13272-017-0245-4

ORIGINAL PAPER

Numerical and experimental investigations of the propeller characteristics of an electrically powered ultralight aircraft

M. Stuhlpfarrer[1] · **A. Valero-Andreu**[1] · **C. Breitsamter**[1]

Received: 22 April 2016 / Revised: 8 February 2017 / Accepted: 8 May 2017 / Published online: 16 June 2017

Abstract The performance and efficiency of a propeller is crucial for electrically powered propulsion systems. Since the energy of the batteries is limited, it is important to develop propellers with high efficiency. Therefore, numerical and experimental investigations of the propeller characteristics are performed. The wind tunnel experiments are performed on a fuselage–propeller configuration. The electrical motor, batteries, and control units are designed to be integrated in the fuselage. Furthermore, force measurements are conducted to provide a data base for the validation of the numerical results. Two different numerical approaches are presented. First, the propeller is fully resolved by applying a rotational domain and a sliding mesh interface. Second, an actuator disk approach including blade element theory with a panel method one-way coupled with a boundary layer integration method is presented. The latter shall be used to reduce computational and mesh generation costs. The thrust, efficiency as well as pressure distribution and the flow field downstream of the propeller are analyzed. The obtained numerical results show a good agreement with the experimental data for the integral values over a wide operating range. Moreover, the results of the inter-method comparison of the two numerical approaches are in a good accordance regarding the local effects for the two highlighted operating points.

Keywords Propeller aerodynamics · High-fidelity simulations · Electric flight · Actuator disk modeling

List of symbols

a_{ij}	Influence coefficient matrix
B	Number of propeller blades
BT	Blade tip
c	Chord length
c_D	Drag coefficient
c_f	Skin friction coefficient
c_L	Lift coefficient
c_p	Pressure coefficient
c_p	Specific heat for constant pressure
c_Q	Torque coefficient
c_T	Thrust coefficient
D	Drag force
D	Diameter
F_φ	Circumferential force
H, H_1	Shape factor
i, j	Indices
J	Propeller advance ratio
k	Turbulence kinetic energy
L	Lift force
l	Variable for Thwaites' model
M_i	Component of the moment
Ma	Mach number
n	Number of cells
n	Rounds per minute
p	Pressure
$p_{\mathrm{in}}, p_{\mathrm{out}}$	Pressure at inlet and outlet
Q	Torque
q	Heat flux
r	Radius
Re	Reynolds number

This paper is based on a presentation at the German Aerospace Congress, September 16–18, 2014, Augsburg, Germany.

✉ M. Stuhlpfarrer
marco.stuhlpfarrer@aer.mw.tum.de

[1] Department of Mechanical Engineering, Chair of Aerodynamics and Fluid Mechanics, Technical University of Munich, Boltzmannstraße 15, 85748 Garching bei München, Germany

S_i	Source term component
T	Thrust
T	Temperature
T_{tot}	Total temperature
U_e	Effective velocity
U_∞	Free-stream velocity
u_∞, v_∞	Free-stream velocity components
u_d	Velocity far downstream of the propeller plane
$u_{\text{ind}}, v_{\text{ind}}$	Induced velocity components
u_i	Component of the velocity
Vol	Volume
V_x	Axial velocity
V_{rel}	Relative velocity
V_r	Radial velocity
V_φ	Circumferential velocity
x, y, z	Cartesian coordinates
x, φ, r	Cylindrical coordinates
y^+	Dimensionless wall distance
ν	Kinematic viscosity
α	Angle of attack
α_{dens}	Density relaxation factor
α_{pres}	Pressure relaxation factor
α_K	Turbulent kinetic energy relaxation factor
α_{mom}	Momentum relaxation factor
α_{temp}	Temperature relaxation factor
$\alpha_{\nu t}$	Turbulence eddy viscosity relaxation factor
α_ω	Turbulence eddy frequency relaxation factor
δ	Boundary layer thickness
δ^*	Displacement thickness
γ	Vortex strength
λ	Thermal conductivity
λ	Variable for Thwaites' model
η	Efficiency
μ	Molecular viscosity
θ	Local angle of incidence
θ_{75}	Angle of incidence at 75 per cent of the blade span
θ	Momentum thickness
ρ	Density
ϕ	Inflow angle
ϕ	Potential
ω	Turbulence eddy frequency

Abbreviations

BET	Blade element theory
RANS/BET	Combined RANS/blade element theory approach
RANS/BET-FC	Combined RANS/blade element theory approach including the fuselage configuration in the wind tunnel test section
RBPA	Reference blade pitch angle
TUM	Technical University of Munich
TUM-AER	Chair of Aerodynamics and Fluid Mechanics
UAV	Unmanned aerial systems
URANS/RP	URANS results for the calculations of the resolved propeller

1 Introduction

The investigations presented herein are part of the integrated research project EUROPAS dealing with an Electric Unmanned Reconnaissance Optionally Piloted Airborne System. The project focuses on technologies for autonomous, unmanned sensor platforms addressing efficient propulsion systems and ground station control technologies. Project partners come from industry, research establishments, and universities while funding is provided by the Bavarian State Ministry of Economic Affairs and Media, Energy and Technology.

The overall objective of the project is to provide solutions for all-electric, environmentally friendly and inexpensive unmanned aerial systems (UAVs) addressing civil and governmental reconnaissance and surveillance tasks. Consequently, the development of certain key technologies as well as an equivalent certification process is required. This activity should promote the first use of ultralight class aircraft in Germany as sensor platforms with optimal load factor with respect to the endurance.

The tasks of the Chair of Aerodynamics and Fluid Mechanics (TUM-AER) of the Technical University of Munich (TUM) concentrate on the adaptation and application of methods of experimental and numerical flow simulation for the analysis and optimization of the aerodynamic performance of the aircraft. In particular, the focus is on the propeller performance and drag minimization to ensure efficient, electrically assisted operations for each flight mission. Numerical simulations and complementary wind tunnel tests are performed, with emphasis on modeling and aerodynamic analysis. The resulting data base provides an essential basis for assessing the achievable flight performance of the electrically powered system and to derive possible optimization potential.

Nowadays, electrically powered flight has attained increased interest caused by the reduced direct pollutant emissions as well as the reduced noise level compared to a combustion engine. Since the first flight of the electrically driven MB-E1 in the year 1973, both endurance and range have been extended [1]. These goals are obtained by the on-going development of batteries and electric engines. The battery's mass-specific energy has increased up to 400 Wh/kg as described in [2–4]. Furthermore, the efficiency of electric motors has been improved to 90% and above as published in [3]. According to [2], enhancement in both battery's mass-specific energy up to 2000 Wh/kg and efficiency of electric motors greater than 93% may be reached by 2030. Nevertheless, the achievable mass-specific energy of batteries remains one order of magnitude less than for liquid fuels. That is why the application is limited to small aircraft at this time. Especially, for ultra-light aircraft, this kind of propulsion system is already feasible. With the aim of increasing the aircraft's range and endurance an efficient propulsion system is required. To fulfill this goal, the propeller aerodynamics has to be optimized also.

The performance of a propeller is depending on a large number of parameters. The presented investigations herein focus on the influence of the blade pitch angle on the thrust and efficiency for various flight regimes. Different experimental and numerical approaches are applied. First, experiments of the fuselage–motor–propeller configuration in the wind tunnel are conducted to generate a reliable data base for validation. Second, simulations solving the unsteady Reynolds-averaged Navier–Stokes equations are performed. Third, a blade element theory approach coupled with the Reynolds-averaged Navier–Stokes (RANS) equations is presented.

2 Experiments

2.1 Aircraft and facility

The wind tunnel tests have been carried out in the large low-speed facility A of the Chair of Aerodynamics and Fluid Mechanics (Aerodynamics Division) of Technical University of Munich. This closed return wind tunnel can be operated with both open and closed test section at maximum usable velocities of 65 and 75 m/s, respectively. Test section dimensions are 1.8 m in height, 2.4 m in width and 4.8 m in length. Because of the aircraft dimensions, the open test section is used. The test section flow was carefully inspected and calibrated documenting a turbulence level of less than 0.4% and uncertainties in the spatial and temporal mean velocity distributions of less than 0.067%. The maximum blockage is 15%.

The experiments are carried out using the real full-scale aircraft without the wing and horizontal tail plane. The main reason is to test the electric propulsion system when installed on the aircraft to get also information on the driving, battery, and cooling characteristics and reliability of the system under free-stream conditions comparable to real flight. Figure 1 shows the geometry and the overall dimensions of the aircraft. The fuselage (including motor and propeller) is sting mounted using a specific cranked sting to connect the wing attachment shaft to the wind tunnel balance mount as presented in Fig. 2. The aircraft is equipped with a three-blade fixed-pitch propeller. The diameter of the propeller is $D = 1.4$ m. Figure 3 shows the airfoil sections at six different radial positions.

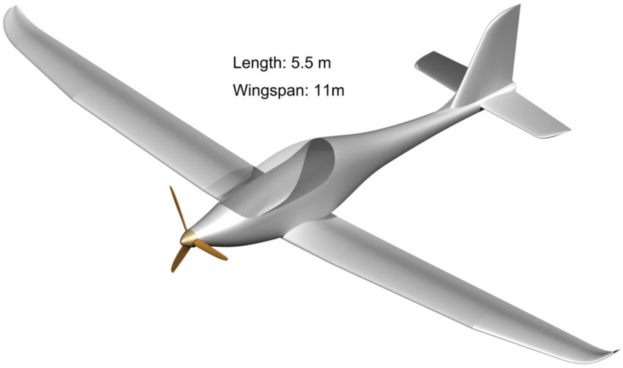

Fig. 1 Airplane geometry and overall dimensions

Fig. 2 Sting-mounted aircraft fuselage in the test section of the wind tunnel A of the Technical University of Munich [26]

2.2 Force measurements and test conditions

An external six-component balance is used to measure the aerodynamic forces and moments acting on the model. Here, the main focus is on the axial force component related to drag and thrust. The balance is designed to sustain maximum loads of ±1500, ±3000 and ±3000 N for axial, lateral, and normal forces, and maximum moments of ±700, ±500 and ±700 Nm for rolling, pitching, and yawing moments, respectively. The load cell accuracy based on maximum loads is 0.025%. Based on the actual loads occurring during the experiments and repeatability tests, the uncertainty in the drag and thrust coefficient is below 3.5%.

The force measurements have been carried out to address real flight conditions, namely at free-stream reference velocities from $U_\infty = 16.67$ m/s to $U_\infty = 33.34$ m/s at ambient pressure p_∞ and ambient temperature

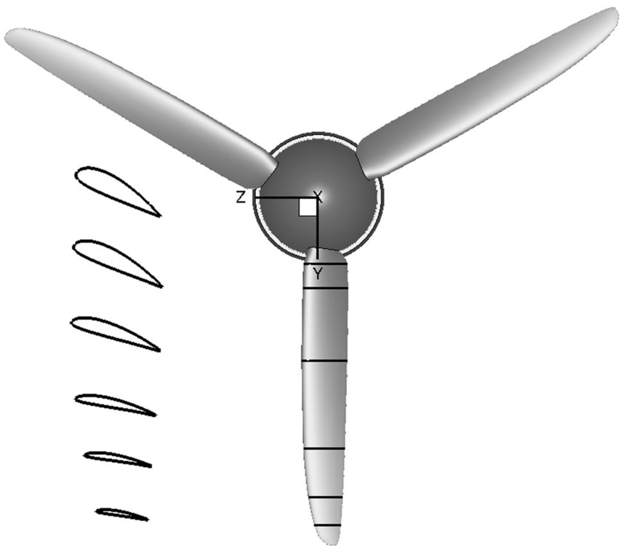

Fig. 3 Front view of the three-bladed propeller including the spinner. Slices of six different airfoil sections are extracted on the left side

T_∞. The uncertainty in the free-stream velocity in the empty test section is less than 0.2%. The corresponding Reynolds numbers based on the chord at 75% span of the propeller blade are in the range of $Re = 4.74 \times 10^5$ to $Re = 7.97 \times 10^5$.

To obtain the net thrust of the propeller, the measured fuselage forces without the propeller are subtracted for each free-stream velocity. The influences of the propeller slipstream and pressure field are not taken into account. The biggest error by the neglect of these effects is expected for operating points with a high thrust value, since the resulting velocity in the propeller wake differs strongly from the free-stream velocity. The maximum error can be approximated by evaluating the velocity difference in the wake field and determining the change in drag from the fuselage measurements without propeller. Since the velocity difference in the wake is not measured, an estimation can be performed by the actuator disk theory [5, 6].

3 Numerical methods

For the investigations, two different numerical methods are applied and described briefly. On the one hand, a finite volume method solving the URANS equations for calculation of the resolved propeller flow is presented (URANS/RP). On the other hand, a combined RANS/blade element theory (RANS/BET) approach is described. For the latter, the main principle of the blade element theory is explained. Additionally, the generation of the required aerodynamic characteristics of the airfoil sections by the application of a linear-strength vortex method in conjunction with a boundary layer integration method is provided.

3.1 URANS calculations

This section gives a brief description of the resolved URANS simulations. Initially, a detailed explanation of the meshing methodology is given. Furthermore, the solver settings are described and at last, a mesh and time step size independency study is presented.

3.1.1 Meshing methodology

The numerical simulations for these investigations are performed with the commercial software ANSYS Fluent. The computational grids are of the block-structured hexahedron type and generated with ANSYS ICEM CFD. The grid is divided into two parts which are connected by sliding mesh interfaces. The sliding mesh interface provides a time-accurate solution between two relative moving mesh parts. Therefore, the adjacent cell faces are intersected and the mass, momentum, and energy fluxes through each resulting face are calculated for every time step [7]. A rotating disk is embedded to model the motion of the propeller while a static domain contains the aft body. Figure 4 shows the propeller configuration used for the numerical simulations. In comparison to the experimental setup, the fuselage and the wind tunnel are excluded for these simulations at this point of the project. The reason for this lies in the reduction of the complexity for the inter-method comparison with the latter described coupled RANS/BET method. Furthermore, it is assumed that the fuselage has only a small influence on the generated thrust. Nonetheless, to avoid wake shedding downstream of the spinner, an aft body is designed. The length and the shape of this aft body are chosen in such a manner that separation should not occur. The dimensionless wall distances to the wall-nearest cell center for no slip walls are set to approximately $y^+ \approx 1$ to resolve the boundary layer behavior without applying a wall function. Furthermore, the number of cells in the boundary layer in the wall-normal direction comprises approximately 20 cells.

Due to the rotational periodicity of the three-bladed propeller, the mesh is generated for a sector of 120° only. Finally, it is rotated and copied twice to obtain the rotating disk mesh which is embedded in the static domain. For stable simulations and to avoid spurious oscillations at the sliding mesh interface, similar cell sizes on both sides are set. Therefore, the edge length ratios are in the order of magnitude of one. The total number of cells in one-third of the rotating disk domain is 2.3×10^6 while the static domain contains 6.4×10^6 cells. The static domain includes 151 blocks and one-third of the rotating domain consists of 598 blocks. Figure 5 shows the mesh of the rotating domain and the propeller blade.

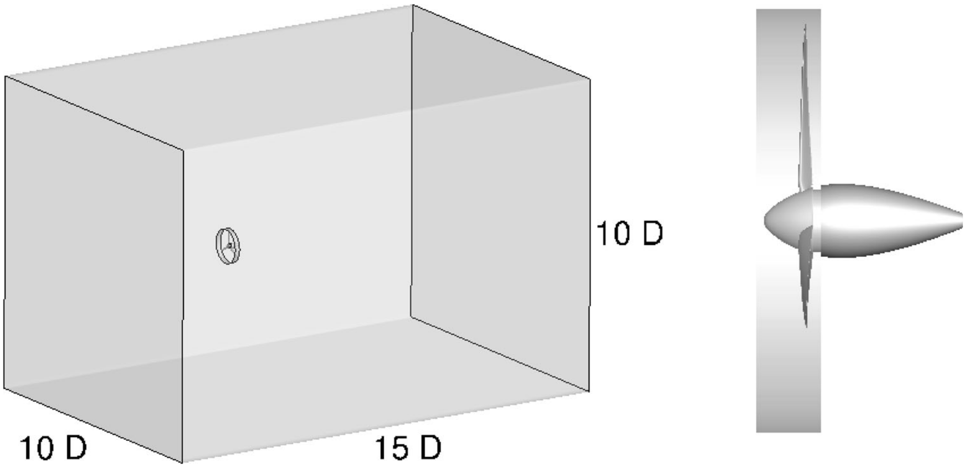

Fig. 4 Static domain with embedded rotating domain (*left*). Side view of the propeller including the aft body and the sliding mesh interface. 1 D is the diameter of the propeller

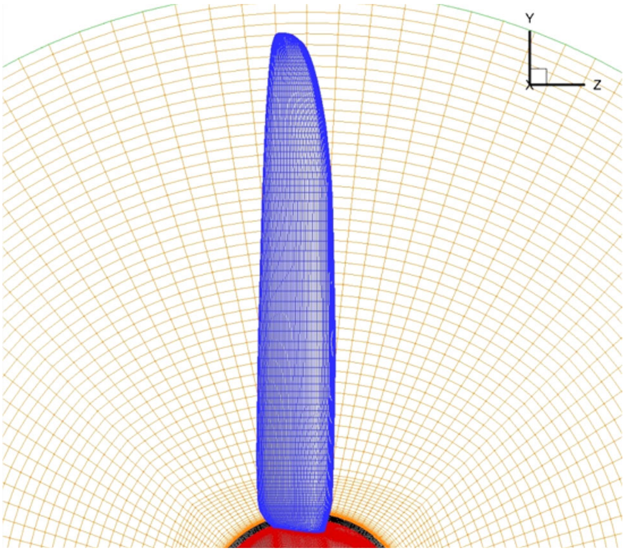

Fig. 5 A detailed view of the surface mesh of the blade is depicted

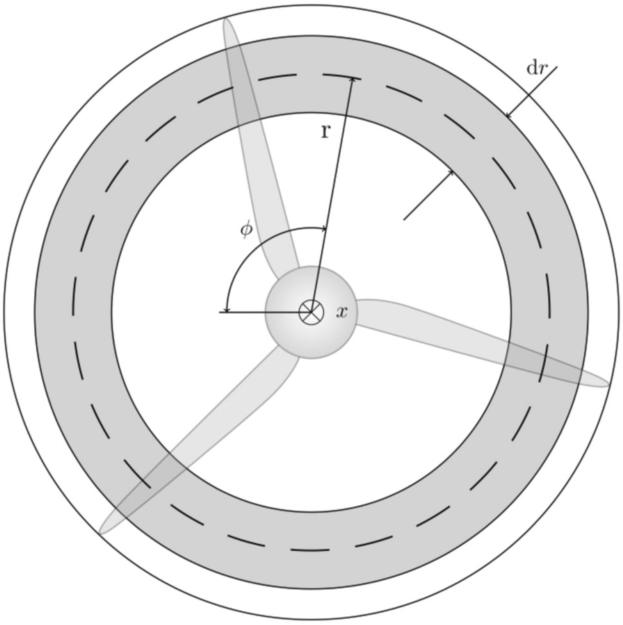

Fig. 6 Blade disk with one highlighted annulus [26]

3.1.2 Solver settings and strategy

The numerical investigations are performed with ANSYS Fluent solving the URANS equations. Regarding the turbulence modelling, the $k-\omega$ shear stress transport (SST) model is applied [8]. Since the blade tip velocities are up to $v_{\mathrm{BT}} = 183$ m/s, the blade tip Mach number is definitely higher than $\mathrm{Ma}_{\mathrm{BT}} > 0.3$. That is why the compressible pressure-based solver is chosen. The velocity formulation in all domains is set to absolute. Furthermore, the calculations are performed in a time-accurate manner to capture the motion of the propeller appropriately. Nevertheless, to speed up the simulations, a steady-state solution is calculated for all different setups as an initial solution in the first step. Subsequently, it is switched to the unsteady solver automatically. The pressure–velocity coupling is treated by applying the SIMPLE algorithm. To reduce the numerical dissipation of the spatial discretization of the momentum, density, and energy, a second-order upwind scheme is chosen. For the temporal discretization, a bounded second-order implicit scheme is used. It blends, depending on the solution, between a first- and a second-order method to prevent spurious oscillations. Moreover, the occurring transport equations for the turbulent kinetic energy as well as the turbulence eddy frequency are discretized by a first-order upwind scheme. Additionally, the least squares cell-based method is used for determining the gradients. The under-relaxation factors for pressure and temperature, α_{pres} and α_{temp}, respectively, are varied during the simulation. Initially, the values are set to $\alpha_{\mathrm{pres}} = \alpha_{\mathrm{temp}} = 0.2$ for the steady-state solution as well as for the first ten time steps in the transient solution. Then the relaxation for the pressure is set to $\alpha_{\mathrm{pres}} = 0.3$ and for the temperature to $\alpha_{\mathrm{temp}} = 1$.

Table 1 Fluid properties and boundary conditions for the numerical simulations are provided

Fluid properties	
Specific heat	$c_p = 1006.43\,\frac{\mathrm{J}}{\mathrm{kg\ K}}$
Molecular viscosity	$\mu = 1.7895 \times 10^{-5}\,\frac{\mathrm{kg}}{\mathrm{m\ s}}$
Thermal conductivity	$\lambda = 0.0242$

Boundary conditions

Boundary type	Velocity	Pressure	Thermal
Inlet	u_∞	$p_{\mathrm{in}} = 101325$ Pa	$T = 293.15$ K
Outlet	–	$p_{\mathrm{out}} = 101325$ Pa	$T = 293.15$ K
Pressure far field	–	$p = 101325$ Pa	$T_{\mathrm{tot}} = 293.15$ K
All physical surfaces	No slip	–	$q = 0\,\frac{\mathrm{W}}{\mathrm{m}^2}$

The under-relaxation factors for the density and turbulence viscosity are set to $\alpha_{\mathrm{dens}} = \alpha_{\nu t} = 0.2$, for the momentum to $\alpha_{\mathrm{mom}} = 0.7$ and for both, the turbulent kinetic energy and the specific dissipation rate to $\alpha_K = \alpha_\omega = 0.8$. The applied fluid is air complying with the ideal gas law. The fluid properties are provided in Table 1. Additionally, for the SST model, viscous heating, compressibility effects as well as a production limiter are included [7].

The prescribed boundary conditions are also shown in Table 1. The turbulence intensity and turbulence viscosity ratio for the inlet are calculated analytically to obtain the same turbulence quantities at the propeller compared to the wind tunnel tests. If reverse flow occurs locally at a far-field boundary condition or at the outlet, the direction of the inflow is obtained by the neighboring cell inside the domain. The turbulence quantities for backflow in the domain are approximately set to the conditions at the propeller. In the case of a backflow into the domain, the pressure is set locally as the total pressure. Furthermore, the non-reflecting acoustic wave model is applied for all pressure far-field boundary conditions. Therefore, the motion of all parts is in compliance with the wind tunnel configuration.

All URANS calculations are performed on the SuperMUC high-performance computing system of the Leibnitz Supercomputing Centre.

3.2 Blade element theory

In this section the blade element theory is described briefly. A detailed derivation can be found in [9]. The blade is divided into several blade sections as shown in Fig. 6. For each of these, force values are determined and thereafter integrated over the whole propeller blade to get thrust and torque values. Figure 7 shows the airfoil for a certain blade section. The geometric pitch angle θ represents the angle between the chord line and the plane orthogonal to the rotation axis. V_x is the axial velocity and V_φ is the circumferential velocity. For axisymmetric inflow conditions, the latter is caused by the circumferential velocity at a given propeller section due to its velocity superimposed by the circumferential inflow component. The addition of the vector components results in the relative velocity vector V_{rel}. Furthermore, the inflow angle ϕ can be determined by

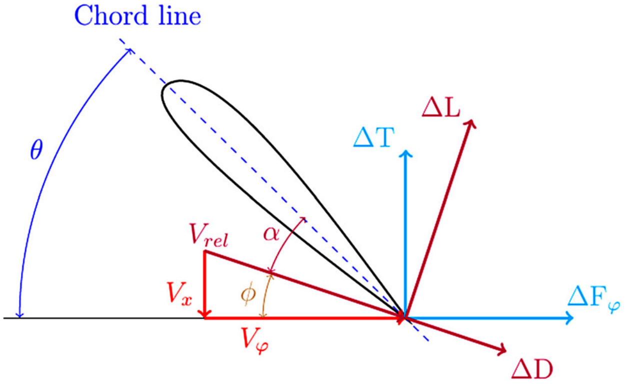

Fig. 7 Blade section with definitions of angles, velocities, and forces [26]

$$\phi = \arctan\left(\frac{V_x}{V_\varphi}\right). \tag{1}$$

Applying this relation, the local angle of attack α at the blade section can be obtained with the inflow angle ϕ as follows:

$$\alpha = \theta - \phi. \tag{2}$$

The lift and drag of a blade section ΔL and ΔD can be expressed by the definition of the respective lift and drag coefficients c_L and c_D as follows:

$$\Delta L = \frac{1}{2}\rho V_{\mathrm{rel}}^2 c_L c \Delta r, \tag{3}$$

$$\Delta D = \frac{1}{2}\rho V_{\mathrm{rel}}^2 c_D c \Delta r. \tag{4}$$

To obtain the thrust and circumferential force for the blade section ΔT and ΔF_ϕ, a change of the reference frame has to be fulfilled that gives

$$\begin{aligned}\Delta T &= \Delta L\cos(\phi) - \Delta D\sin(\phi)\\ &= \frac{1}{2}\rho V_{rel}^2 c(c_L\cos(\phi) - c_D\sin(\phi))\Delta r,\end{aligned} \tag{5}$$

$$\begin{aligned}\Delta F_\phi &= \Delta L\sin(\phi) + \Delta D\cos(\phi)\\ &= \frac{1}{2}\rho V_{\mathrm{rel}}^2 c(c_L\sin(\phi) + c_D\cos(\phi))\Delta r.\end{aligned} \tag{6}$$

These equations provide the thrust and circumferential force for the blade section of one propeller blade. To take the number of propeller blades B into account both equations have to be multiplied with B. The propeller thrust and torque are obtained by summing over all blade sections

$$T = \sum \Delta TB = \sum \frac{1}{2} \rho V_{\text{rel}}^2 c(c_L \cos(\phi) - c_D \sin(\phi)) B \Delta r, \tag{7}$$

$$\begin{aligned} Q &= \sum \Delta F_\phi B r \\ &= \sum \frac{1}{2} \rho V_{\text{rel}}^2 c(c_L \sin(\phi) + c_D \cos(\phi)) B r \Delta r. \end{aligned} \tag{8}$$

It becomes evident that for evaluating these relations the lift and drag coefficients c_L and c_D have to be known. The relation to determine these coefficients will be provided in the following section. Furthermore, some characteristic parameters for the propeller are introduced. These are the thrust coefficient, torque coefficient, advance ratio, and efficiency, respectively,

$$C_T = \frac{T}{\rho n^2 D^4}, C_Q = \frac{Q}{\rho n^2 D^5}, J = \frac{V_\infty}{nD}, \eta = \frac{J}{2\pi} \frac{C_T}{C_Q}. \tag{9}$$

3.3 Linear-strength vortex method

As mentioned above, the lift and drag coefficients for each section have to be known. To determine these coefficients, a linear-strength vortex panel method is implemented to solve the incompressible potential flow equations [10]. A short overview of the method is provided in Appendix A.1.

3.4 Boundary layer integral method

Since the panel method is not able to calculate the viscous drag, another modelling approach has to be employed. For this purpose, a boundary layer integration method is used. For these investigations a one-way coupling between the panel method and a boundary layer integral method (PanBL) is applied for simplicity. The approach is based on [11].This means that at first, the inviscid potential flow around the airfoil is calculated. Second, the resulting boundary layer parameters are integrated in downstream direction and finally, the drag coefficient c_D is obtained. However, there is no feedback of the calculated boundary layer displacement thickness to the panel method. A short overview of the method is provided in Appendix A.2. The Prandtl–Glauert compressibility correction is applied to the described panel method. Additionally, the Java-Foil stall correction [12] is applied to approximate the effect of the separation on lift and drag. This is implemented into a C-code that is coupled with ANSYS Fluent presented in the following section.

3.5 Blade element theory/finite volume method—coupling

Especially, in the field of wind turbines the coupling of blade element theory and a finite volume method, solving the Navier–Stokes equations, is applied to reduce computational effort as shown in [13–17] for steady and unsteady flows. As explained above, the blade element theory in combination with the PanBL determines the thrust and circumferential force of the blade section. The inputs for these methods are the local angle of attack and the inflow velocity magnitude for the blade section. The inflow velocity components for the axisymmetric flow are obtained by a cell-volume weighted averaging over the annulus at the actuator disk position. For non-axisymmetric flows, each annulus could be divided into several sectors to capture, for example, skewed flows as well. For this purpose, a coordinate transformation into the cylindrical coordinate frame has to be performed for all cells which are located in the disk according to

$$\begin{pmatrix} V_x \\ V_r \\ V_\varphi \end{pmatrix}_{\text{cyl}} = \begin{pmatrix} 1 & 0 & 0 \\ 0 & -\cos(\varphi) & -\sin(\varphi) \\ 0 & \sin(\varphi) & -\cos(\varphi) \end{pmatrix} \begin{pmatrix} u \\ v \\ w \end{pmatrix}_{\text{cart}}. \tag{10}$$

For the investigations, a cell is counted to be part of the disk if its cell center is located in the region of the disk. For the x-velocity component in one section of the disk with N_{cis} cells, it is obtained by

$$V_x = \frac{\sum_{N_{\text{cis}}} V_{x,c} \text{Vol}_c}{\sum_{N_{\text{cis}}} \text{Vol}_c}. \tag{11}$$

The same procedure is performed for the other two components. Additionally, the implementation for a parallel computation requires summing over all compute nodes. With this information, the local speed of the blade can be determined and is used for the PanBL. With the resulting lift and drag coefficients, lift and drag for each section with the appropriate velocities and chord lengths are determined. The density is set constant for the coupled approach since it is assumed that the compressibility effects are covered by the Prandtl–Glauert transformation within PanBL. The generated forces are normalized with the volume of the annulus to obtain specific volume forces at each section. Between the sections, linear interpolation depending on the radial position is used for determining the specific lift and drag as well as the local inflow angle. Latter is used for the coordinate frame transformation to obtain the specific thrust and the circumferential force in the cylindrical coordinate system as follows:

$$\begin{pmatrix} T \\ F_\varphi \end{pmatrix}_{\text{cyl}} = \begin{pmatrix} \cos(\phi) & -\sin(\phi) \\ -\sin(\phi) & -\cos(\phi) \end{pmatrix} \begin{pmatrix} L \\ D \end{pmatrix}_{\text{cyl}}. \tag{12}$$

Finally, the specific thrust and the circumferential force have to be further transformed to the Cartesian coordinate frame and will be written as volumetric source terms for the momentum equations

$$\begin{pmatrix} S_x \\ S_y \\ S_z \end{pmatrix}_{\text{cart}} = \begin{pmatrix} 1 & 0 & 0 \\ 0 & -\cos(\varphi) & \sin(\varphi) \\ 0 & -\sin(\varphi) & -\cos(\varphi) \end{pmatrix} \begin{pmatrix} T \\ 0 \\ F_\varphi \end{pmatrix}_{\text{cyl}}. \tag{13}$$

For this purpose, the source terms provided in ANSYS Fluent can be coupled directly with the output quantities generated by PanBL. Regarding the incompressible Navier–Stokes equation in differential form, the momentum equation with the added source term reads

$$\frac{\mathrm{d}u_i}{\mathrm{d}t} + u_j \frac{\mathrm{d}u_i}{\mathrm{d}x_j} = -\frac{1}{\rho}\frac{\mathrm{d}p}{\mathrm{d}x_i} + \frac{\mathrm{d}}{\mathrm{d}x_i}\left(\nu \frac{\mathrm{d}u}{\mathrm{d}x_j}\right) + S_i. \tag{14}$$

As stated above, incompressible equations are used, since the compressibility effects are assumed to be modeled appropriately by the Prandtl–Glauert transformation.

3.5.1 *Mesh methodology and solver settings for the coupled method*

To allow an adequate comparison between the different approaches, the meshing strategy and distribution of the blocks and nodes are identical to the URANS/RP setup for the static domain. Nevertheless, the blocking strategy for the inner propeller domain has to be changed. On the one hand, because of the method's principle it is not needed to resolve the propeller anymore and on the other hand, the sliding mesh interface can be omitted. As a consequence, the preparation and the meshing process can be simplified drastically. Furthermore, the numerical effort for solving the flow at the sliding mesh interface is reduced as well.

The solver settings and chosen models are based on URANS simulations. Due to the circumferential averaging the RANS/BET approach allows a steady-state solution. Therefore, the relaxation factors are set according to the steady-state pre-solution for the URANS calculations. Since the incompressible solver is applied, the energy equation is not solved and the density in the field is set to 1.2 kg/m^3. Moreover, the boundary conditions are the same as described for the URANS simulations.

3.6 Mesh and time step independency study

This section includes the mesh independency studies for the URANS/RP and for the coupled RANS/BET approach. For the URANS/RP, a systematic variation of the grid size as well as the time step size is performed to check if the solution is independent with respect to both parameters. The target value is the thrust coefficient. The calculations are performed for a free-stream velocity of $v = 16.67$ m/s and a rotational speed of $\omega = 209.44$ rad/s at a reference blade pitch angle (RPBA) of $\theta_{75} = 10°$ defined at 75% of the tip radius. The RANS/BET approach requires a mesh independency study only, since it is a steady-state simulation.

The study for the URANS/RP simulation includes three different grid sizes and five different times step sizes. The coarse mesh contains 6.9 Mio. cells, the medium 12.9 Mio. cells and the finest 25 Mio. cells. For the independency study the rotating disk domain as well as the static domain is refined systematically. The time step sizes are in accordance with an azimuthal angle per time step of 0.25°, 0.5°, 1°, 2°, and 4°. The thrust evaluation is performed by different averaging procedures. The mean thrust values taken for periods of two, one and, a half propeller revolution and the actual value are calculated to assess the convergence. For a fully converged result the averaged results shall give similar values. Due to the computational effort of these simulations, a small number of propeller revolutions shall be obtained. Since the deviation between the one and the half propeller revolution averaged values after five propeller revolutions is in the order of magnitude of minus four, it is decided to choose five propeller revolutions for the simulations. Figure 8 shows the thrust coefficient of the one revolution averaged thrust coefficient. It shows that there is still a slight tendency for reducing the thrust depending on the time step size. Nevertheless, due to the computational effort it is decided to use a 2° time step per revolution and the middle mesh. Consequently, the deviation of the thrust coefficient is less than one per cent compared to the finest time step size mesh resolution combination. Therefore, the chosen mesh and time step size is fully adequate.

The mesh independency study for the RANS/BET method includes three different mesh sizes as described above. The meshes in the outer region are equal to the

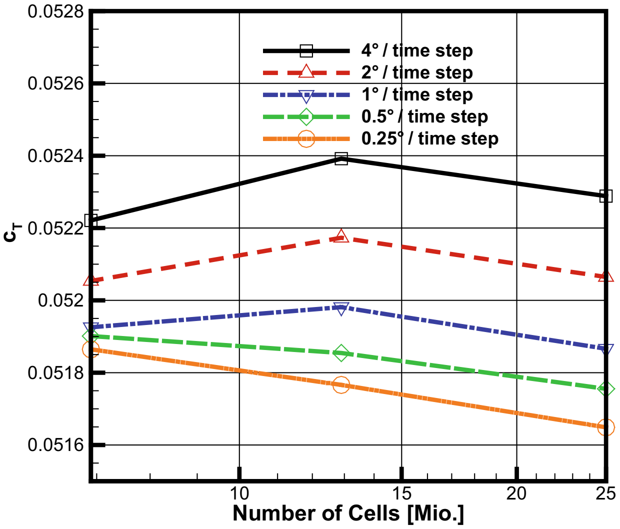

Fig. 8 Mesh and time step size independency study for the URANS/RP as a function of the number of cells

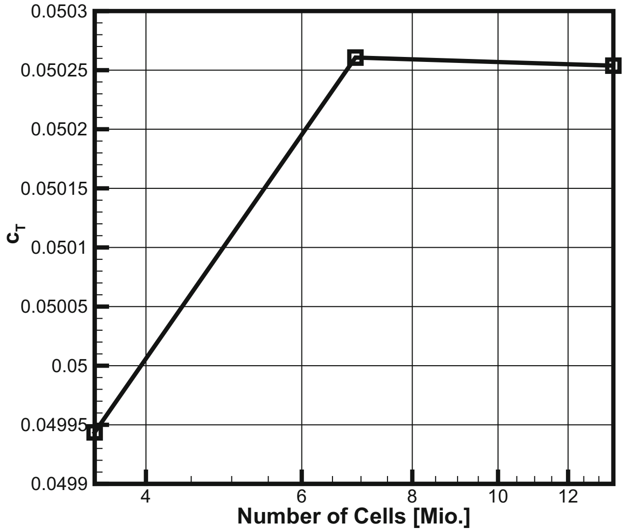

Fig. 9 Mesh independency study for the RANS/BET. The thrust coefficient C_T is shown as a function of the number of cells

URANS/RP simulations. Figure 9 shows the thrust coefficient for the different meshes. There it is depicted that the difference between the coarse and the fine mesh is less than one per cent of the thrust coefficient. Nevertheless, since for the unsteady calculation the medium mesh is chosen for comparison issues, it is used for these investigations as well.

3.7 Numerical *W/T*-fuselage configuration

As a further step, numerical investigations of the measured configuration shall be conducted to obtain the influence of the *W/T* boundaries on the results. For this purpose, the configuration as shown in Fig. 10 is used. The *W/T* includes the nozzle, the diffusor, collector blades, and the test section. Within the test section the fuselage is mounted on a vertical sting. The grid for the numerical simulation is a block-structured mesh containing 3382 blocks and 5.7 Mio. hexahedron cells. The mesh for the fuselage in the test section is embedded into the wind tunnel mesh and connected by a stationary interface. The chosen models are the same as for the above-described simulations of the RANS/BET approach. Furthermore, the velocity at the exit of the nozzle is set to the values measured in the experiment.

4 Results and discussion

In the following, the results of the URANS/RP simulations and the RANS/BET calculations are compared to the experimental data. First, the integral coefficients such as the thrust and torque coefficients and the resulting efficiency over the whole parameter range are compared. Second, the obtained blade loading for the different numerical methods is described and at last, the wake flow of the propeller is analyzed.

4.1 Thrust and efficiency

The most interesting quantities in the course of this project are the thrust and efficiency of the propeller. In Fig. 11 the thrust coefficient C_T depending on the advance ratio J is presented for $\theta_{75} = 8°$, $\theta_{75} = 10°$, $\theta_{75} = 12°$, and $\theta_{75} = 14°$ for the wind tunnel experiment, the URANS/RP simulations as well as the RANS/BET approach. Furthermore, the results of the RANS simulations of the fuselage in the *W/T* applying the BET (RANS/BET-FC) for the propeller are shown. To estimate the deviation of the results with and without the fuselage, a flight condition with a comparatively small advance ratio of $J = 0.318$ is taken. Therefore, the RPBA is $\theta_{75} = 10°$, the rotational speed is $\omega = 235.62$ rad/s and the free-stream velocity is $U_\infty = 16.67$ m/s. The thrust coefficient obtained by the experiment for this case reads $c_T = 0.059$. After

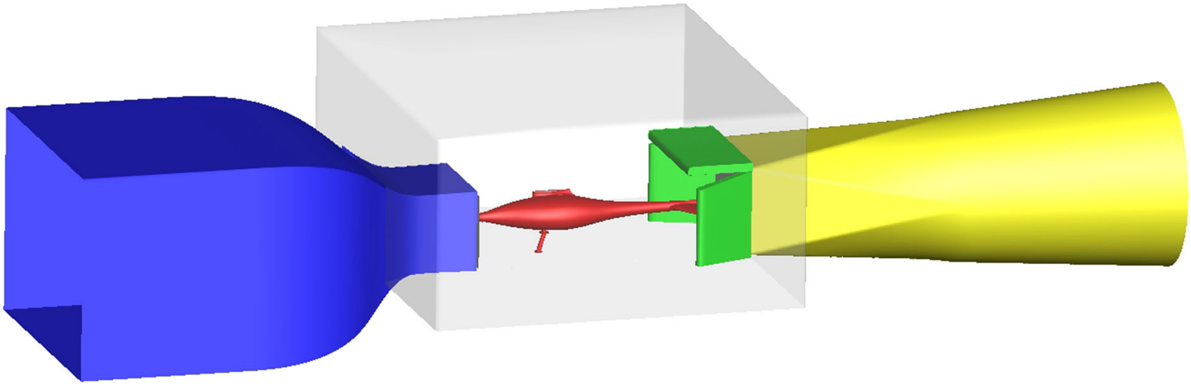

Fig. 10 Computational domain for the simulation including the *W/T*. The aircraft is mounted by a mounting sting (*red*) in the test section. Nozzle (*blue*), diffusor (*yellow*), and the collector blades are contained in the setup also

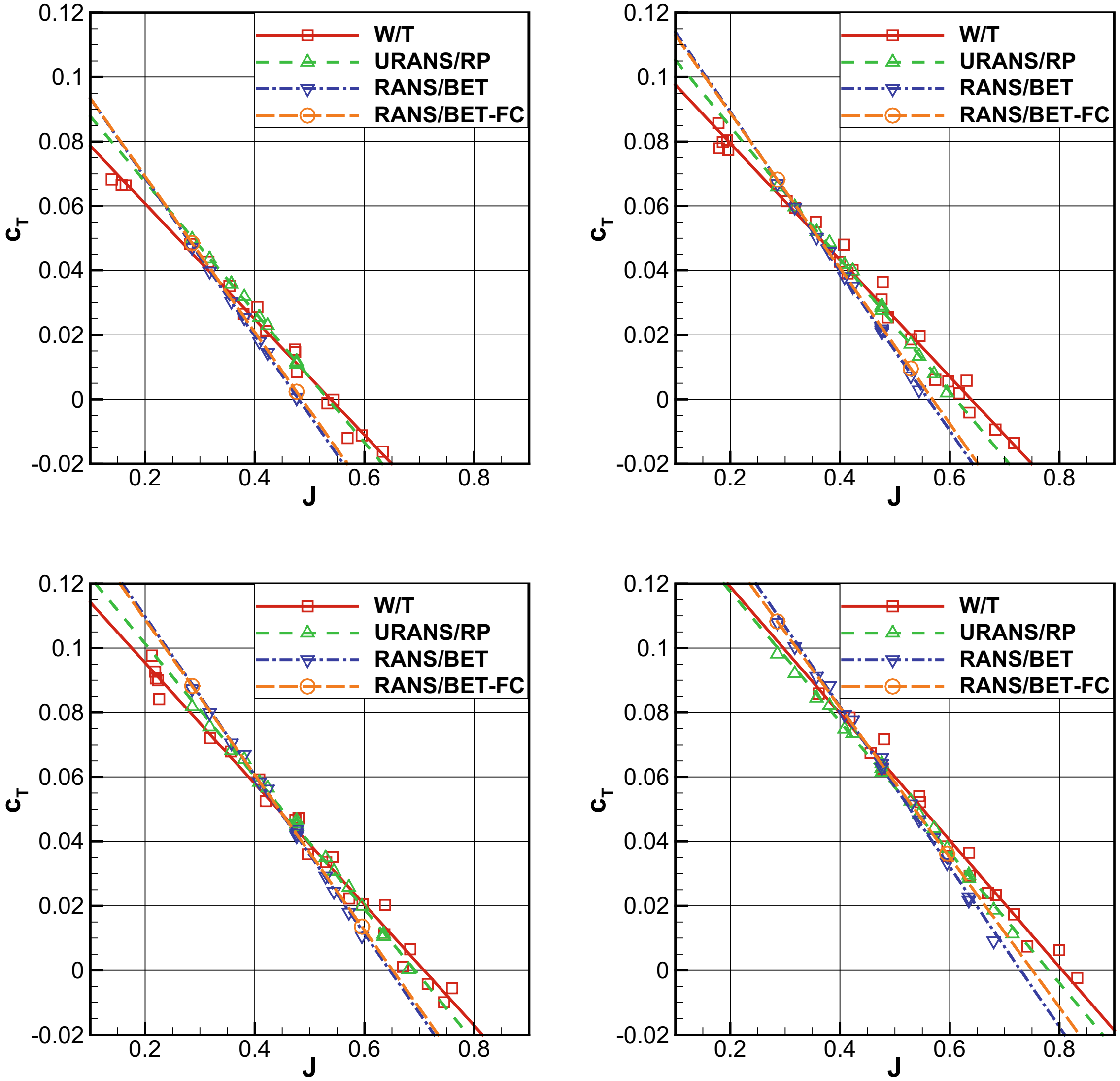

Fig. 11 Thrust coefficient C_T as a function of the advance ratio J for $\theta_{75} = 8^\circ$, $\theta_{75} = 10^\circ$, $\theta_{75} = 12^\circ$, and $\theta_{75} = 14^\circ$

subtracting the drag of the fuselage from the measured overall force consisting of propeller thrust and fuselage drag, and using the actuator disk formulation, the velocity far downstream of the propeller can be determined as $u_d = 26.39$ m/s. Interpolating the measured drag of the fuselage for u_d and correcting the drag of the fuselage for u_d, a thrust coefficient of $c_T = 0.065$ is obtained. This shows an underestimated thrust coefficient for small advance ratios up to 10% by the applied procedure. If the thrust coefficient gets smaller, the influence caused by the slipstream is reduced. This effect leads to a larger slope of c_T with respect to J. Moreover, the small distance to the floor of the *W/T* test section influences the thrust of the disk that can be hardly determined. Therefore, the numerical simulation applying RANS/BET with the fuselage in the *W/T* is performed. The CFD results are created for the presence of the fuselage following the methodology applied for the experimental results (aerodynamic tare). The thrust coefficient for this operating point reads $c_T = 0.061$. Compared to the experimentally obtained values of $c_T = 0.059$ the deviation is approximately 3.5%. Nevertheless, the actual thrust coefficient differs. For the RANS/BET-FC result it is $c_T = 0.066$, while the RANS/BET result gives $c_T = 0.060$. The difference in the thrust is obtained since the RANS/BET-FC includes the interference effects of the propeller with the fuselage and the test section. Comparing the slope of c_T with respect to J between the RANS/BET and the RANS/BET-FC gives a good agreement as shown in Fig. 11. The reason is that for smaller advance ratios the thrust obtained by the RANS/BET-FC is bigger as stated above but the drag of the fuselage is also higher because of the propeller slipstream. These counteracting effects lead to a nearly similar slope of c_T with respect to J. In addition, the numerical simulations are conducted for the cruise

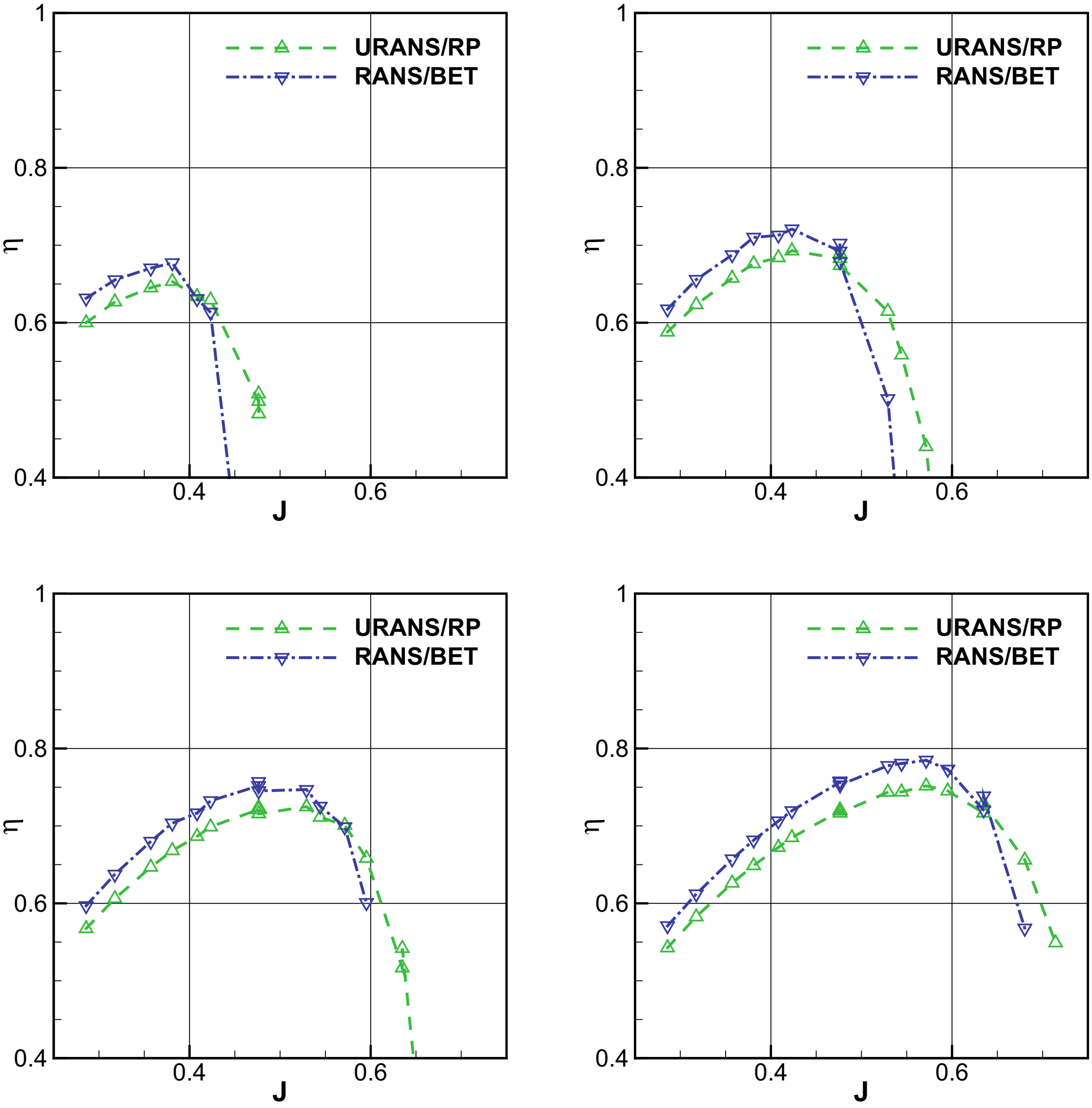

Fig. 12 Efficiency η as a function of the advance ratio J for $\theta_{75} = 8°$, $\theta_{75} = 10°$, $\theta_{75} = 12°$, and $\theta_{75} = 14°$

flight condition described in detail below. The RBPA is $\theta_{75} = 14°$, the rotational speed is $\omega = 209.44$ rad/s and the free-stream velocity is $U_\infty = 27.78$ m/s. The experimentally obtained thrust coefficient is $c_T = 0.038$ while the numerical solution gives $c_T = 0.036$. It is shown that there is also a good agreement between numerical and experimental results.

The symbols represent the simulated thrust coefficient values, whereas the lines are obtained by a linear fit. However, the slope of c_T with respect to J is varying between the approaches. The wind tunnel data show the largest slope and the URANS/RP shows the smallest slope. The URANS/RP simulation is in very good agreement with the wind tunnel data over the whole operating range. The RANS/BET approach shows a larger discrepancy. Especially, for high advance ratios J the thrust is underestimated. Nevertheless, both numerical approaches show good results for the conditions with moderate blade loading.

Table 2 Description of the test cases is provided

Test case	RPBA	Rotational speed	Free-stream velocity	Advance ratio
Climb flight	$\theta_{75} = 10°$	$\omega = 261.80$ rad/s	$U_\infty = 16.67$ m/s	$J = 0.286$
Cruise flight	$\theta_{75} = 14°$	$\omega = 209.44$ rad/s	$U_\infty = 27.78$ m/s	$J = 0.595$

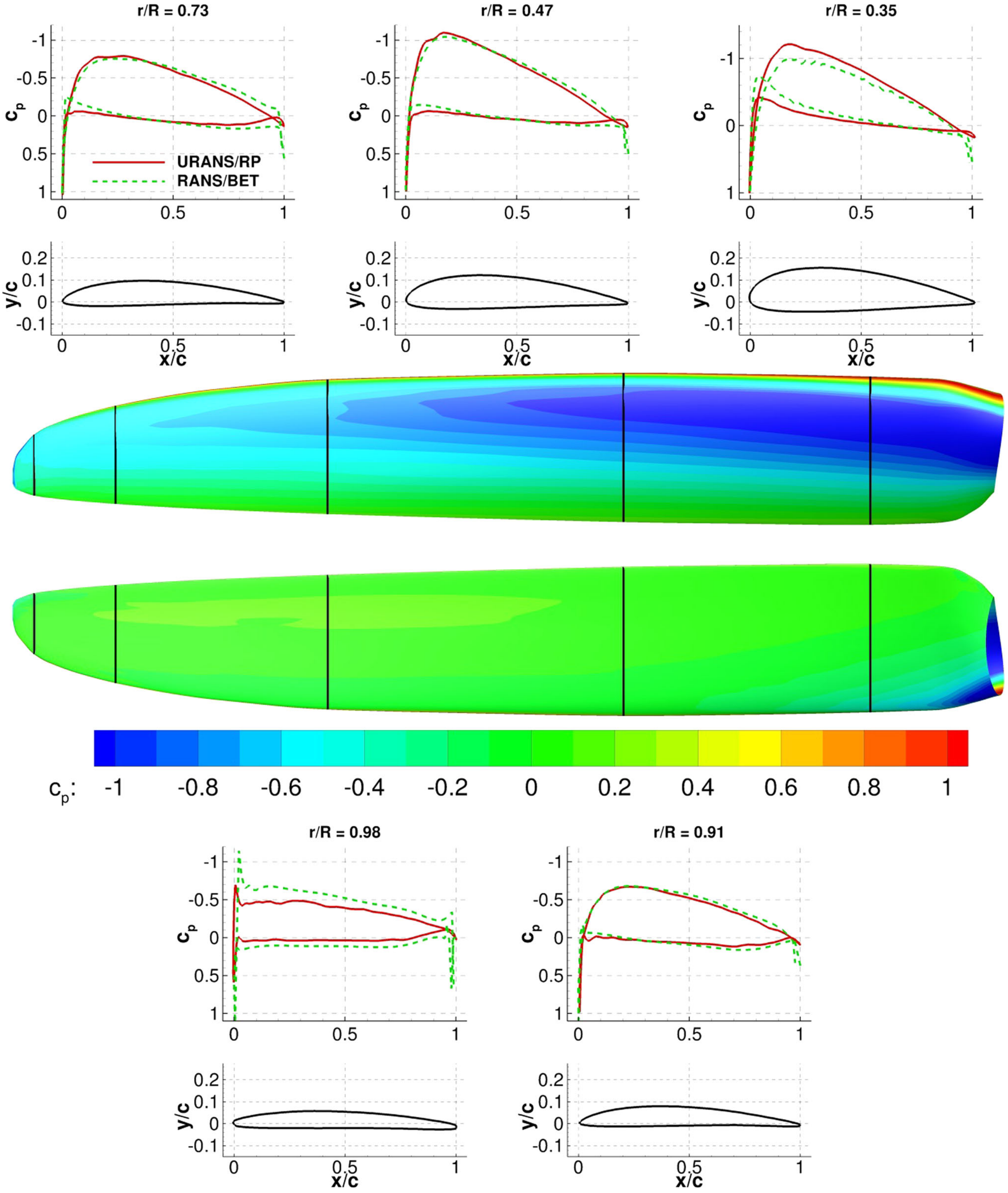

Fig. 13 Blade pressure distribution for the climb flight regime obtained by URANS/RP (*middle*). Pressure distribution at five radial sections resulting from the URANS/RP and RANS/BET solution; $v = 16.67$ m/s, $\omega = 261.80$ rad/s, $\theta_{75} = 10°$

Figure 12 shows the efficiency η of the propeller depending on the advance ratio J for $\theta_{75} = 8°$, $\theta_{75} = 10°$, $\theta_{75} = 12°$, and $\theta_{75} = 14°$. Here, only the numerical results are presented, since the torque obtained from the wind tunnel experiment is influenced strongly by the slipstream of the propeller interacting with the vertical stabilizer. It is shown that the RANS/BET approach overestimates the maximum efficiency for all RBPAs compared to the URANS/RP but the qualitative behavior is comparable. In particular, the maximum efficiency is predicted at the same advance ratio J. The biggest difference is obtained for high advance ratios J where the RANS/BET drops below the result of the URANS/RP simulation. This occurs in the range of high advance ratios J where the blade loading is small and the thrust of the propeller is underestimated, although the torque of the propeller is predicted to be too small as well for higher advance ratios by the RANS/BET. Nevertheless, the reduced zero thrust advance ratio causes this effect.

Considering a maximum deviation from the wind tunnel experiment of $c_T = c_{T,WT} \pm 0.01$, all thrust coefficients obtained with the URANS/RP calculations are within this range, Fig. 11. The RANS/BET results are within this range for an advance ratio of $0.17 \leq J \leq 0.48$, $0.20 \leq J \leq 0.53$, $0.24 \leq J \leq 0.62$, and $0.25 \leq J \leq 0.65$ for the RBPA of $\theta_{75} = 8°$, $\theta_{75} = 10°$, $\theta_{75} = 12°$, and $\theta_{75} = 14°$, respectively. For certain points the deviation is less than $c_T = c_{T,WT} \pm 0.001$ for both methods. The important fact is that the region of high efficiency is captured well. One URANS/RP simulation needs approximately 7 h on 168 cores calculated on SuperMUC. The RANS/BET can be calculated on a workstation in half an hour on 6 cores. Therefore, the latter is approximately 400 times faster than the URANS/RP.

4.2 Blade loading

For assessing the local prediction quality of the RANS/BET, the blade loading at certain propeller span sections is compared to the related URANS/RP result. Therefore, the pressure distribution is discussed and, furthermore, the sectional lift coefficient is described. Two cases assigned to different flight regimes are chosen as provided in Table 2.

At first, the climb flight is discussed. This condition is marked by a high blade loading and a small advance ratio. The obtained averaged thrust coefficient for this case from the URANS/RP result is $c_T = 0.0659$ with an efficiency of $\eta = 0.588$. The RANS/BET approach provides a $c_T = 0.0672$ with an efficiency of $\eta = 0.642$. This point is chosen due to the maximum available power of the engine. Figure 13 shows the pressure coefficient distribution at the suction and pressure side of the blade as contour plot obtained by the URANS/RP simulation. Additionally, for five radial sections the pressure coefficient depending on the chord length is presented for the URANS/RP simulation as well as the RANS/BET approach. It is visible that both approaches show qualitatively and quantitatively a good agreement for all presented sections. In a more detailed consideration, it is remarked that the pressure peak at the pressure side is overestimated by the RANS/BET. This effect is much more pronounced for the sections with a smaller radial position due to the reduced angle of attack.

In the following, the thrust coefficients for the sections along the blade span are evaluated and compared for the different approaches. The sectional thrust coefficient is defined as follows:

$$\Delta c_T = \frac{\Delta T}{\rho D^4 n^2}. \tag{15}$$

In this equation, ΔT represents the generated section thrust, n is the rotational speed of the propeller and D the diameter of the propeller. Figure 14 shows the distribution of the sectional thrust coefficient for both approaches. A good agreement between both results is obtained. Slight differences in the blade tip region can be determined. In this region, the vorticity of the blade tip vortex sheet obtained by the RANS/BET approach is too small compared to the vorticity of the blade tip vortices of a resolved propeller blade. The reduced vorticity is caused by the spatial distribution of the thrust on the whole disk surface compared to the resolved propeller where it acts on the surface of the blade. Thus, the induced velocity is underestimated which leads to a higher thrust in this region.

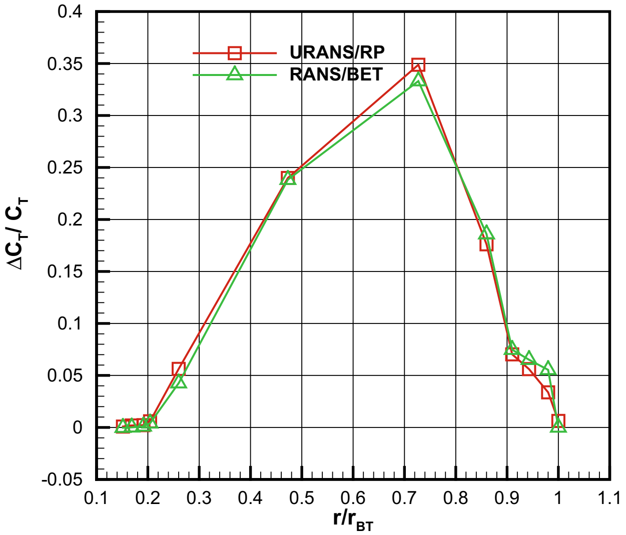

Fig. 14 Sectional thrust coefficient (climb flight regime) resulting from the URANS/RP and RANS/BET solution

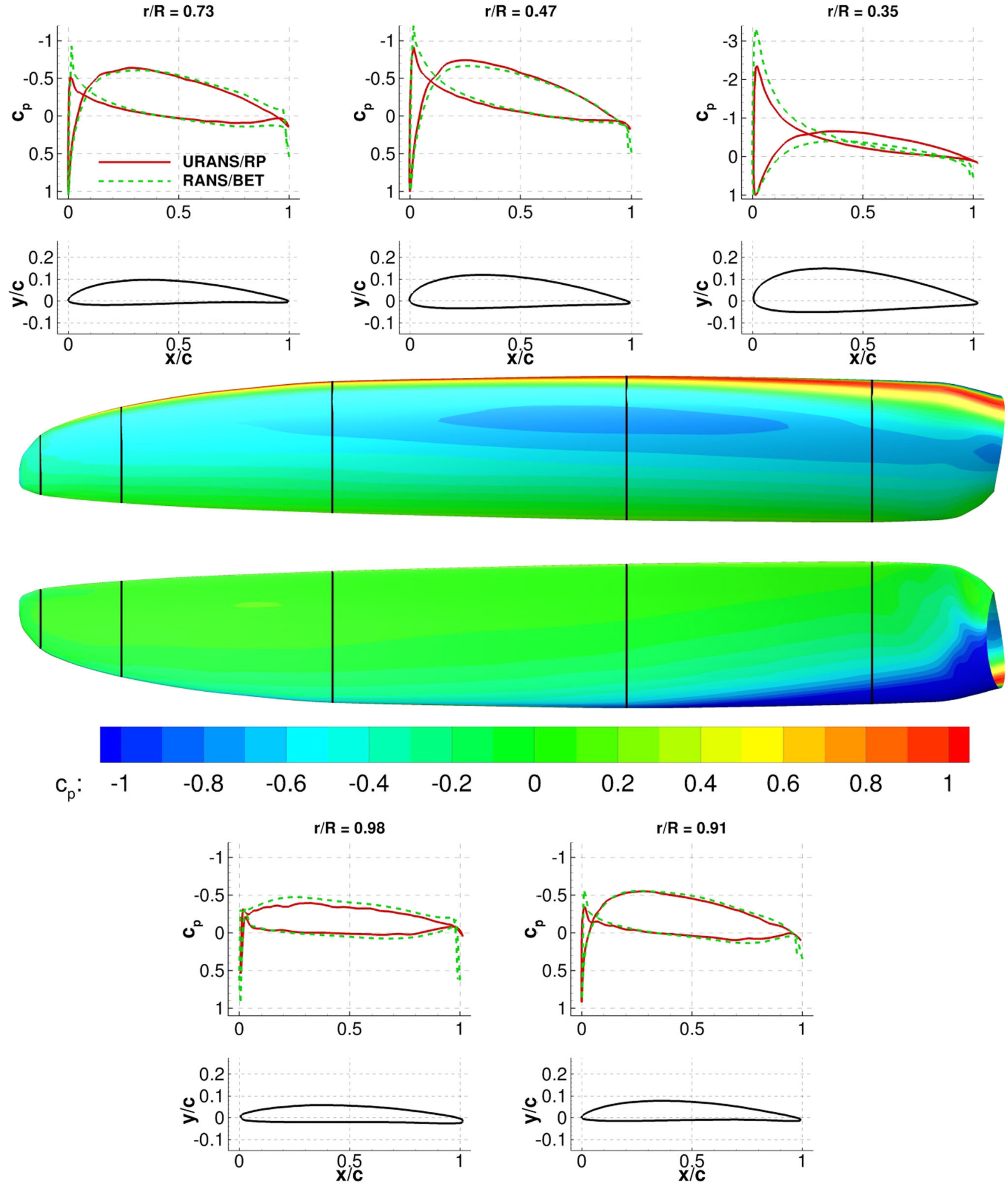

Fig. 15 Blade pressure distribution for the cruise flight case obtained by URANS/RP (*middle*). Pressure distribution for five radial sections resulting from the URANS/RP and RANS/BET solution; $v = 27.78$ m/s, $\omega = 209.44$ rad/s, $\theta_{75} = 14°$

Second, the appropriate parameters for the cruise flight test case are shown in Table 2. The thrust coefficient obtained by URANS/RP is $c_T = 0.0379$ and from the RANS/BET approach it gives $c_T = 0.0335$. Figure 15 shows the pressure distribution in the same manner as presented for the climb flight case above. The overall

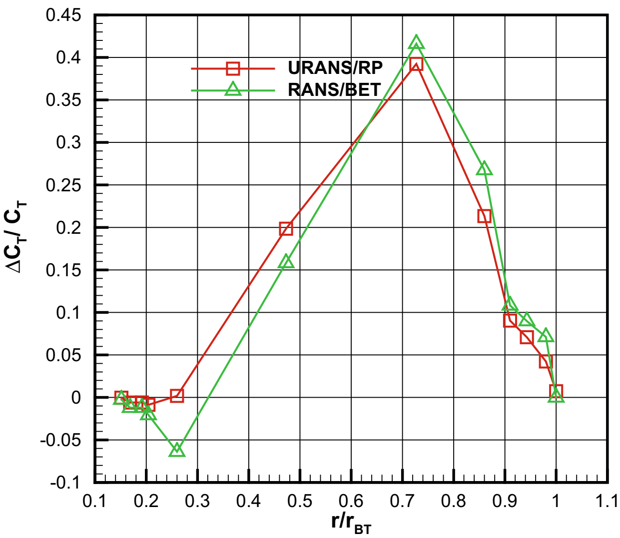

Fig. 16 Sectional thrust coefficient (cruise flight regime) resulting from the URANS/RP and RANS/BET solution

accordance between the URANS/RP and the RANS/BET pressure distribution is good. Nevertheless, the above-described effect of the overestimated negative pressure peak at the pressure side of the propeller blade has increased. The reason for this occurrence is, first, that in this region the flow is separated which is not appropriately covered by the RANS/BET modelling approach. Second, the inflow velocity vector for the sections in the RANS/BET approach is assumed to be perpendicular which is not valid in this region. Considering the sectional thrust coefficient for this flight regime, the effect of the negative thrust in the region near the spinner is also depicted in Fig. 16. Nevertheless, in the blade tip region there is still a good agreement between both results. From an integral point of view, the underestimated thrust coefficient can also be explained with this result.

4.3 Wake analysis

To evaluate the RANS/BET flow field downstream of the propeller, the velocity field at defined downstream positions is compared to the corresponding URANS/RP result. The same flight regimes as above are considered (Table 2). Initially, the result for the climb flight case is discussed. Figure 17 depicts the time-averaged normalized axial velocity distribution for the URANS/RP and the RANS/BET result. The contour plot shows qualitatively good accordance between both approaches for the upstream as well as the downstream velocity field of the propeller. Differences occur in the wake flow of the aft body due to a more upstream located separation for the actuator disk approach. The separation is caused by the reduced axial momentum in the boundary layer downstream of the actuator disk. Since the resolved propeller disturbs the flow *B* times per revolution and the actuator disk reduces the momentum continuously, the averaged velocity field downstream of the propeller remains attached. Additionally, it has to be mentioned that for the URANS/RP result the velocity field in the rotational frame is averaged. That is why the influence of the blade tip vortex is visible in the solution. Furthermore, at the domain interfaces a discontinuity appears in the contour plot. For a quantitative discussion, the normalized axial velocity distribution along the radius at three different downstream positions is provided. A good agreement is achieved as well. Since linear interpolation is chosen for determining the strength of the source terms between the sections, a discrepancy between both methods in the wake flow is obtained. Concerning the previously mentioned interaction with the boundary layer, the differences in the wake downstream of the aft body separation can be addressed. The velocity deficit in the aft body wake flow is increased due to the upstream separation along the symmetry line.

For the cruise flight case, similar illustrations are provided in Fig. 18. The qualitative comparison on the basis of the contour plot shows a good agreement downstream of the propeller. Differences can be detected upstream of the spinner. The quantitative comparison along the radial lines downstream of the propeller emphasizes that the blade tip region is predicted well compared to the URANS/RP simulation. Discrepancies occur at smaller radial positions induced by the underestimated thrust coefficient provided by PanBL for the corresponding blade sections. Moreover, the aft body wake flow differs as well due to the above-described interaction with the momentum of the boundary layer.

The numerical effort for the RANS/BET is the same as provided for the thrust coefficient above. For the URANS/RP simulations ten propeller revolutions are calculated to obtain a converged wake flow field for a downstream distance of three propeller diameters. Consequently, the RANS/BET is approximately 800 times faster for the wake calculations than the URANS/RP while providing a reasonable accuracy with respect to the time-accurate URANS/RP results.

5 Conclusions

In the course of the integrated research project EUROPAS, numerical and experimental investigations on the propeller characteristics of an ultralight aircraft were performed. Wind tunnel experiments were conducted for operational

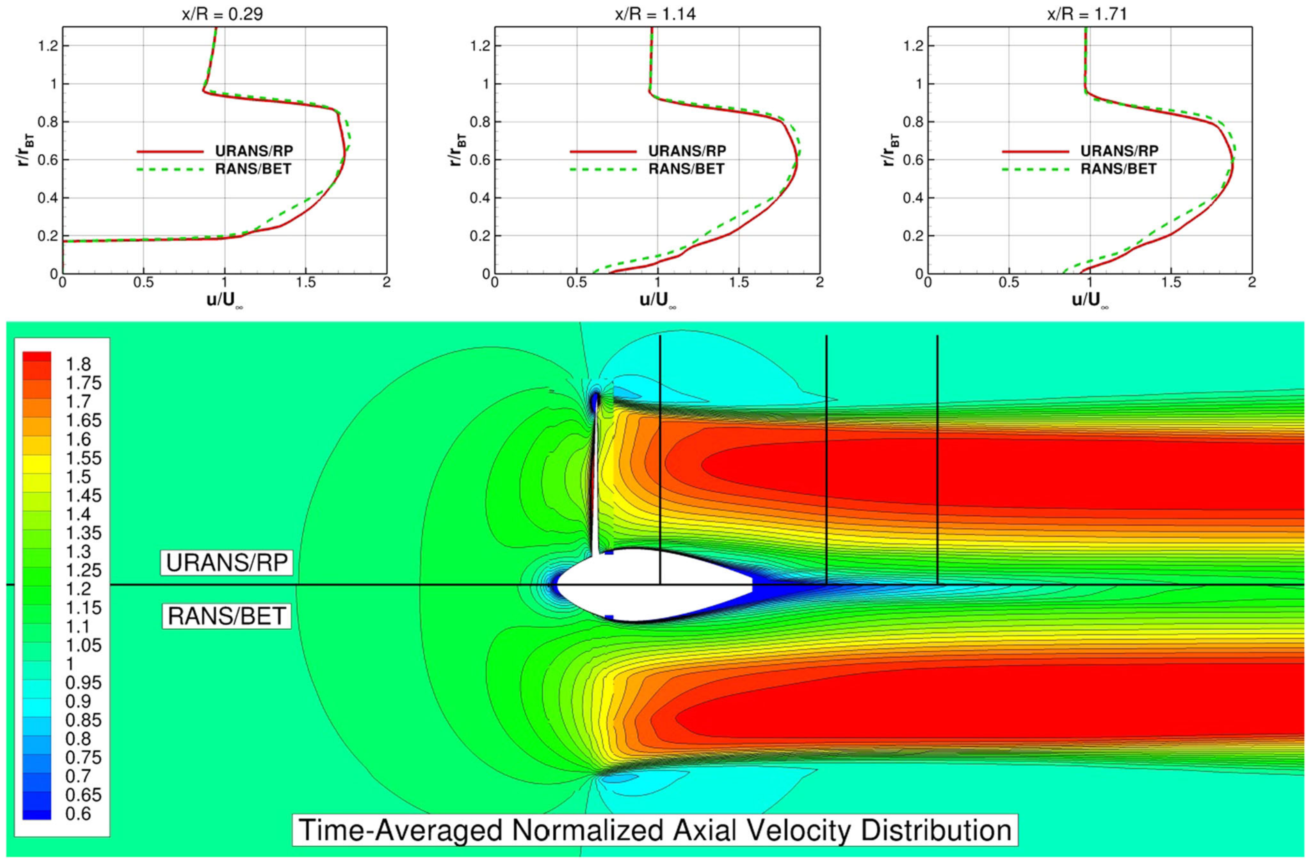

Fig. 17 Contour plot of the time-averaged normalized axial velocity for the URANS/RP and RANS/BET result (*bottom*). Radial distribution of the normalized axial velocity at three different positions downstream of the propeller in climb flight regime; $v = 16.67$ m/s, $\omega = 261.80$ rad/s, $\theta_{75} = 10°$

issues and to obtain a validation data set for the numerical investigations. Two numerical approaches were compared in the course of this project. First, the resolved propeller flow was calculated with URANS and, second, the URANS simulation used an actuator disk approach with the disk loading obtained by PanBL. The latter is a panel method combined with a boundary layer integration method. The objective of the coupled approach was to reduce the computational effort in terms of avoiding the sliding mesh interfaces. Moreover, grid generation time for meshing the propeller can be prevented as well.

The resulting integral coefficients obtained by the numerical simulation were validated with the wind tunnel data. A very good agreement between URANS/RP and the experimental data was obtained. The RANS/BET provides a slightly different slope for c_T as a function of J. Nevertheless, the numerical results are in good accordance with wind tunnel data by three orders of magnitude less numerical effort. Furthermore, the efficiency of the propeller was investigated. The RANS/BET overestimates the efficiency in a wide range of the advance ratio compared to the URANS/RP but the advance ratio for the maximum efficiency is predicted right. For assessing the local prediction capability the pressure coefficient distribution and the sectional lift coefficient were discussed. Two different flight regimes were chosen for the discussion, the climb flight and the cruise flight. The inter-method comparison shows a good agreement as long as the flow remains attached. For separated flows, the applied stall model may not be fully appropriate for all flow conditions. This especially affects the spinner region for high advance ratios where negative sectional thrust coefficients are produced. Consequently, the thrust coefficient is underestimated. Finally, the wake field obtained by the RANS/BET approach was compared to the URANS/RP approach. This point is of major interest for further investigations in the course of this project to determine the interaction of the propeller wake field with the fuselage. The qualitative and quantitative comparison shows good accordance of the wake flow field, especially for the cruise flight case.

To enhance the quality of the RANS/BET results the modelling of the blade itself can be further improved. In the course of this project the next step will be to perform simulations for non-axial inflow with this coupled approach.

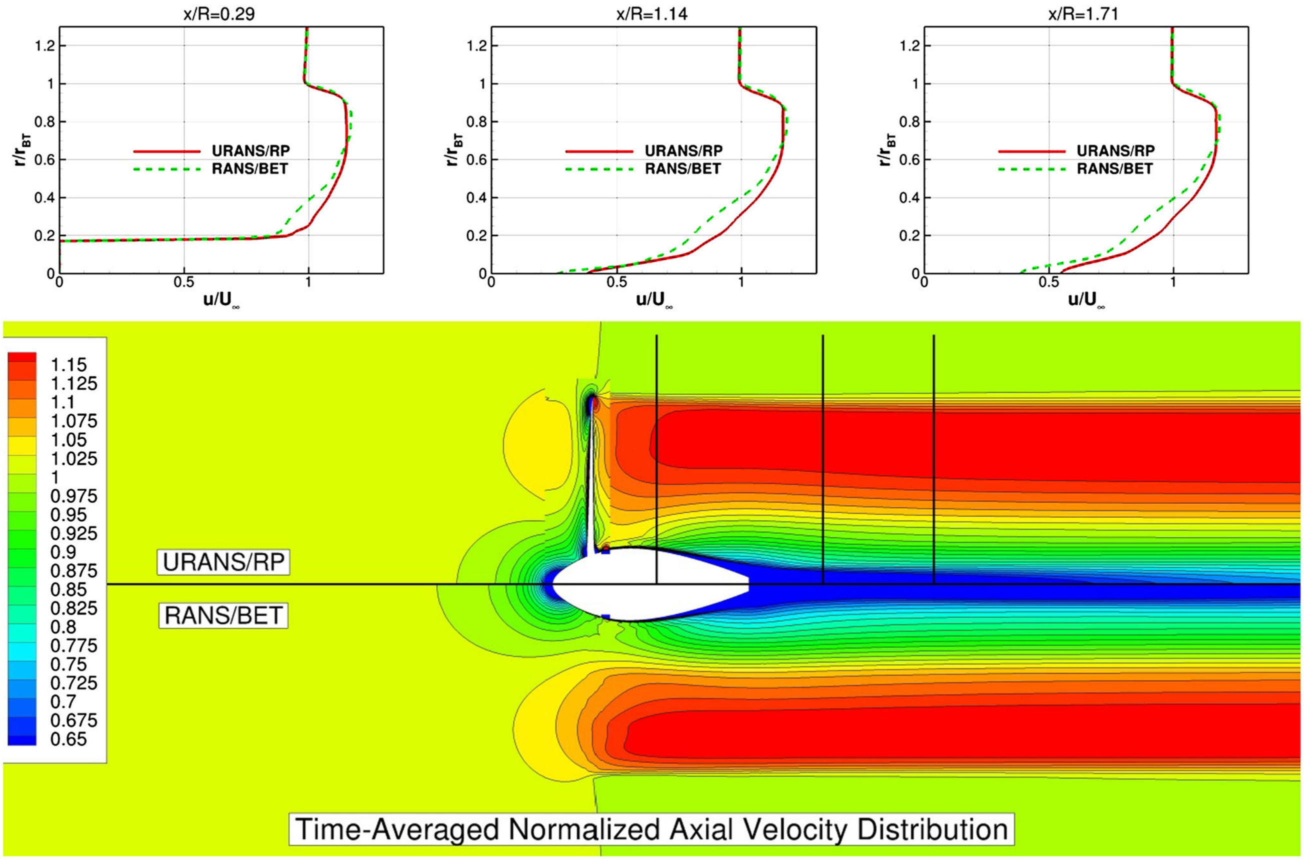

Fig. 18 Contour plot of the time-averaged normalized axial velocity for the URANS/RP and RANS/BET result (*bottom*). Radial distribution of the normalized axial velocity at three different positions downstream of the propeller in cruise flight regime; $v = 27.78$ m/s, $\omega = 209.44$ rad/s, $\theta_{75} = 14°$

Acknowledgements The authors thank the Bavarian State Ministry of Economic Affairs and Media, Energy and Technology for funding the project EUROPAS under the Grant Agreement Number LABAY76A. Furthermore, the authors want to thank ANSYS for providing the flow simulation software. The authors gratefully acknowledge the Gauss Centre for Supercomputing e.V. (www.gauss-centre.eu) for funding this project by providing computing time on the GCS Supercomputer SuperMUC at Leibniz Supercomputing Centre (LRZ, www.lrz.de).

Appendix A.1

In this section the linear-strength vortex panel method is presented according to [10]. For the boundary conditions the impermeability constraint is fulfilled by applying a Neumann boundary condition that reads as follows:

$$u_n = \frac{\partial \phi}{\partial n} = 0. \tag{16}$$

In this formulation the vector n represents the surface orthogonal vector. The potential ϕ_P at a certain field point $P(x, y)$ can be determined out of the free-stream potential ϕ_∞ and the potential originating from the distribution of vortices with the strength ϕ_V at the boundary of the airfoil and gives the following relation:

$$\phi_P = \underbrace{u_\infty x + v_\infty y}_{\phi_\infty} + \int_S \underbrace{\frac{\gamma}{2\pi}\theta \mathrm{d}s}_{\phi_V}. \tag{17}$$

Combining this with the Neumann boundary condition and dividing the airfoil into n panels as depicted in Fig. 19 for each panel leads to

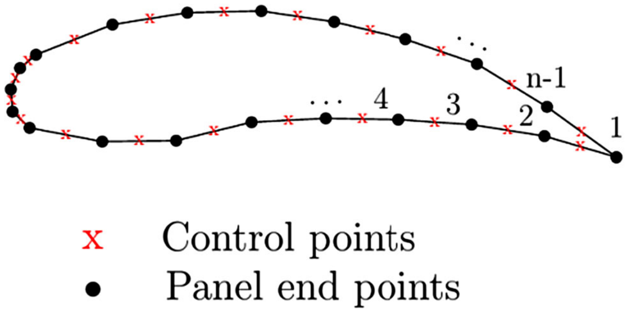

Fig. 19 Panel end points and control points [26]

$$(u_\infty, v_\infty)\cdot n + \sum_{i=1}^{n} \int\limits_{S_p} \frac{\partial \phi_V}{\partial n}\,\mathrm{d}s = (u_\infty, v_\infty)\cdot n + (u_{\mathrm{ind}}, v_{\mathrm{ind}})\cdot n = 0. \tag{18}$$

In this context,u_{ind} and v_{ind} are the induced velocity components due to the influences of the vortex distribution at a certain panel. As mentioned above, the linear-strength vortex distribution is applied. Therefore, the vortex strength in the local panel coordinate system is defined as $\gamma(x_p) = \gamma_0 + \gamma_1 \cdot x_p$. The induced velocity components in the panel coordinate system including this relation are

$$\begin{aligned} u_p = {} & \frac{y_p}{2\pi}\left(\frac{y_{j+1}-y_j}{x_{j+1}-x_j}\right)\ln\frac{r_{j+1}}{r_j} \\ & + \frac{\gamma_j\left(x_{j+1}-x_j\right)+\left(\gamma_{j+1}-\gamma_j\right)\left(x_p-x_j\right)}{2\pi\left(x_{j+1}-x_j\right)}\left(\theta_{j+1}-\theta_j\right), \end{aligned} \tag{19}$$

$$\begin{aligned} v_p = {} & -\frac{\gamma_j\left(x_{j+1}-x_j\right)+\left(\gamma_{j+1}-\gamma_j\right)\left(x_p-x_j\right)}{2\pi\left(x_{j+1}-x_j\right)}\, ln\frac{r_j}{r_{j+1}} \\ & + \frac{y_p}{2\pi}\left(\frac{y_{j+1}-y_j}{x_{j+1}-x_j}\right)\left[\frac{x_{j+1}-x_j}{y_p} + \left(\theta_{j+1}-\theta_j\right)\right]. \end{aligned} \tag{20}$$

These equations are applied to all panels and after redistribution and transformation into the global coordinate system the influence coefficient matrix is obtained as follows:

$$a_{ij} = (u, v)_{i,j}\cdot n_i. \tag{21}$$

This finally leads to a set of N algebraic equations with the right-hand side

$$\mathrm{RHS}_i = -\left(U_{\infty}, V_{\infty,}\right)\cdot(\cos\alpha_i, -\sin\alpha_i). \tag{22}$$

Additionally, the Kutta condition on the trailing edge is included that reads

$$\gamma_1 + \gamma_{N+1} = 0. \tag{23}$$

The resulting system is solved by applying a LU decomposition with partial pivoting (PLU). The reason for this is the numerical stability and the low computational effort of $O\left(\frac{2}{3}n^3\right)$ compared to other methods. With the obtained vortex distribution the local tangential velocity at each panel can be solved easily. Using this result the pressure coefficient distribution can be calculated by applying

$$c_p = 1 - \frac{U_e}{U_\infty}. \tag{24}$$

and finally after summation and coordinate frame rotation the lift and drag coefficients are obtained.To show the results obtained by PanBL briefly, they are compared to Xfoil results [25]. Therefore, simulations for the Naca0012 airfoil are performed at a $Re = 5 \times 10^5$. Furthermore, the flow is considered to be incompressible. Figure 20 shows the lift coefficient as a function of the angle of attack. For smaller angles both results are in good agreement. Especially, in the stall region differences can be detected since the PanPL result overestimates the lift coefficient. This is caused by the applied stall model. Furthermore, Fig. 21 shows the drag coefficient as a function of the angle of attack. Therefore, both results coincide well for smaller angles. Nevertheless, in the stall region PanBL result overestimates the Xfoil results in the range of 14° $<\alpha<$ 17°.

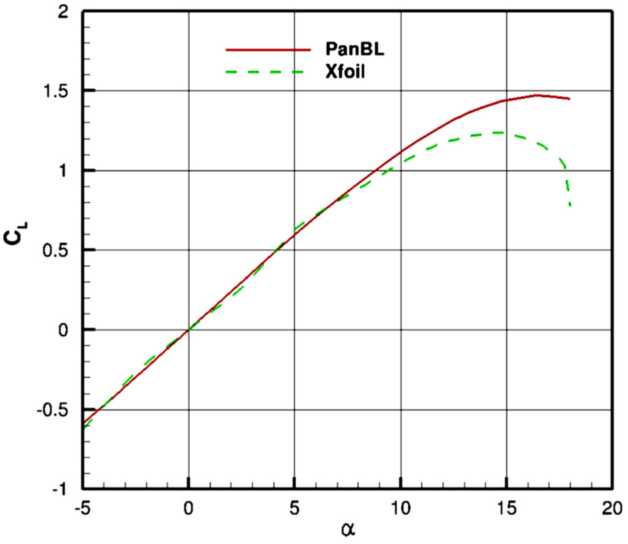

Fig. 20 C_{L} as a function of α for the Naca0012 airfoil obtained by PanBL and XFOIL for a $Re = 5 \times 10^5$

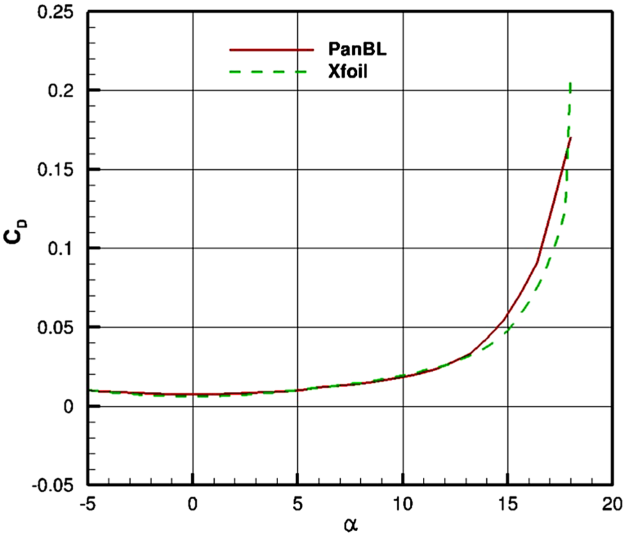

Fig. 21 C_{D} as a function of α for the Naca0012 airfoil obtained by PanBL and XFOIL for a $Re = 5 \times 10^5$

Appendix A.2

The applied boundary layer integration method uses a similar formulation as described in [11]. Using Prandtl's boundary layer equations for incompressible flow [18], combining them into one integral equation which is solved along the y-direction from $y = 0$ to $y \to \infty$ the Kármán integral momentum equation is obtained and by introducing the shape factors H it reads

$$\frac{\mathrm{d}\theta}{\mathrm{d}x} + \frac{\theta}{U_e}(2+H)\frac{\mathrm{d}U_e}{\mathrm{d}x} = \frac{1}{2}C_f. \tag{25}$$

Multiplying (25) with $\frac{\theta U_e}{\nu}$ and substituting $L = \frac{\theta U_e}{\nu}\frac{C_f}{2}$ and $\lambda = \frac{Re\theta^2}{\nu}\frac{dU_e}{dx}$ leads to

$$\frac{U_e}{\nu}\frac{\mathrm{d}^2\theta}{\mathrm{d}x^2} = 2(L - (2+H)\lambda). \tag{26}$$

With Thwaites' [19, 20] approach approximating the right-hand side with $2(L - (2+H)\lambda) \approx 0.45 - 6\lambda$ gives

$$\frac{1}{\nu}\frac{\mathrm{d}}{\mathrm{d}x}(\theta^2 U_e^6) = 0.45U_e^5. \tag{27}$$

With the known value at the stagnation point this equation can be integrated along the airfoil streamwise direction by a fifth-order Gaussian quadrature. By the knowledge of θ, λ can be determined. Using the semi-empirical formulas of Cebeci and Bradshaw [20], $H(\lambda)$ and $C_f(\lambda)$ can be estimated. The latter is only used to check if laminar separation occurs. In this case, the calculation starting from the separation point will be performed with the model for turbulent boundary layers. Additionally, Michel's criterion [21] for transition will be used if laminar separation is not detected. Therefore, it is assumed that transition takes place when reaching a specific Reynolds number based on the distance from the stagnation point. The criterion reads

$$Re_\theta > Re_{\theta\mathrm{krit}} = 1.174\left(1 + \frac{22400}{Re_x}\right)Re_x^{0.46}. \tag{28}$$

For the turbulent boundary layer, Head's model is used [23]. Within this model the volume rate of fluid in the boundary layer at the streamwise position x is combined with the definition of the displacement thickness that leads to

$$\delta^* = \delta - \int_0^{\delta(x)} \frac{u(x,y)}{U_e}\mathrm{d}y. \tag{29}$$

With the shape factor H_1 and according to the experimental data from Cebeci and Bradshaw [20], the following equations are obtained:

$$\frac{1}{U_e}\frac{\mathrm{d}}{\mathrm{d}x}(U_e\theta H_1) = 0.0306(H_1 - 3)^{-0.653}, \tag{30}$$

$$H_1 = \begin{cases} 3.3 + 0.8234(H - 1.1)^{-1.287} & \text{if } H \leq 1.6 \\ 3.3 + 1.5501(H - 0.6778)^{-3.064} & \text{if } H \geq 1.6. \end{cases} \tag{31}$$

The skin friction can be computed by the Ludwig–Tillman skin friction law [23]:

$$C_f = 0.246 \times 10^{-0.678H} \cdot \mathrm{Re}_\theta^{-0.268}. \tag{32}$$

These equations are integrated along the airfoil up to the trailing edge or in the case of turbulent separation to the point of separation. The drag coefficient is determined by the Squire–Young [25] formula that reads

$$\begin{aligned} C_D = {} & [2(\theta_{\mathrm{TE}}/c)(U_e/U_\infty)_{\mathrm{TE}}^{\frac{H_{\mathrm{TE}}+5}{2}}]_{\mathrm{UP}} \\ & + [2(\theta_{\mathrm{TE}}/c)(U_e/U_\infty)_{\mathrm{TE}}^{\frac{H_{\mathrm{TE}}+5}{2}}]_{\mathrm{DOWN}}. \end{aligned} \tag{33}$$

References

1. Hepperle, M.: electric flight–potential and limitations. In: AVT-209 workshop on energy efficient technologies and concepts operation, Lissabon (2012)
2. Diouf, B., Pode, R.: Potential of lithium-ion batteries in renewable energy. Renew. Energy **76**, 375–380 (2015)
3. Kumar, L., Jain, S.: Electric propulsion system for electric vehicular technology: a review. Renew. Sustain. Energy Rev. **29**, 924–940 (2014)
4. Froude, JGe: A review of lithium and non-lithium based solid state batteries. J. Power Sources **282**, 299–322 (2015)
5. Froude, R.: On the part played in propulsion by difference pressure. Trans. Inst. Naval Archit. **30**, 390–423 (1889)
6. Rankine, W.: On the mechanical principles of the action of propellers. Trans. Inst. Naval Archit. **38**(3), 13–39 (1865)
7. ANSYS, Inc.: "ANSYS academic research, release 16.0, help system", (2016)
8. Menter, F.R.: Two-equation Eddy-viscosity turbulence models for engineering applications. AIAA J. 32(8), 1598–1605 (1994)
9. Glauert, H.: "Airplane propellers," in aerodynamic theory, pp. 169–360. Springer, Berlin (1935)
10. Katz, J., Plotkin, A.: Low-speed aerodynmics. McGraw-Hill, New York (1991)
11. Wauquiez, C.: Shape optimization of low speed airfoils using matlab and automatic differentiation. Stockholm (2000)
12. Hepperle, M.: "JavaFoil," [Online]. Available: http://www.mh-aerotools.de. Accessed 20 Apr 2016
13. Sorensen, J., Kock, C.: A model for unsteady rotor aerodynamics. J. Wind Eng. Ind. Aerodyn. **58**, 259–275 (1995)
14. Sorensen, J., Myken, A.: Unsteady actuator disk model for horizontal axis wind turbines. J. Wind Eng. Ind. Aerodyn **58**, 139–149 (1992)
15. Sorensen, J., Shen, W.: Analysis of wake states by a full-field actuator disc model. Wind Energy **1**, 73–88 (1998)
16. Madsen, H.: A CFD analysis of the actuator disc flow compared to momentum theory results. In: 10th IEA Symp. on the Aerodynmics of Wind Turbines, Edinburgh, (1996)

17. Mikkelsen, R.: Actuator disc methods applied to wind turbines. DTU-Tryk, Lyngby (2003)
18. Houghton, E.L., Carpenter, P.W.: Aerodynamics for engineering students. Elsevier Butterwoth-Heinemann, Oxford (2003)
19. Thwaites, B.: Approximate calculation of the laminar boundary layer. Aeronaut Quart **1**, 245 (1949)
20. Cebeci, T. and Bradshaw, P.: Momentum transfer in boundary layers. Hemisphere Publishing Corporation, Washington (1977)
21. Michel, R.: Étude de la transition sur les profils d'aile. Tech. rep. 1/1578A ONERA (1951)
22. Head, M.R.: Entrainment in the turbulent boundary layers, ARC Technical Report R & M No 3152. Her Majesty's Stationery Office, London (1958)
23. Ludwieg, H. and Tillmann, W.: Investigations of the wall shearing stress in turbulent boundary layers, Technical Memorandom 1285. NACA, Washington (1950)
24. Squire, H.B. and Young, A.D.: The calculation of the profile drag of airfoils, R & M No 1838. HMSO, London (1937)
25. Drela, M. and Youngren, H.: XFOIL subsonic airfoil development system, [Online]. Available: http://web.mit.edu/drela/Public/web/xfoil/. Accessed 22 July 2016
26. Stuhlpfarrer, M., et al.: Numerical and experimental investigation of the propeller characteristics of an electrically powered ultralight aircraft in DLRK, Augsburg. Deutsche Gesellschaft für Luft- und Raumfahrt - Lilienthal-Oberth e.V. (2014)